PMMA-templating generation and high catalytic performance of chain-like ordered macroporous LaMnO₃ supported gold nanocatalysts for the oxidation of carbon monoxide and toluene

Yuxi Liu, Hongxing Dai*, Jiguang Deng, Lei Zhang, Baozu Gao, Yuan Wang, Xinwei Li, Shaohua Xie, Guangsheng Guo

Laboratory of Catalysis Chemistry and Nanoscience, Department of Chemistry and Chemical Engineering, College of Environmental and Energy Engineering, Beijing University of Technology, Beijing, 100124, PR China

ABSTRACT

Rhombohedrally crystallized chain-like LaMnO₃ and its supported gold (xAu/LaMnO₃; x = 1.4, 3.1, and 4.9 wt%) catalysts have been prepared using the poly(ethylene glycol)-assisted polymethyl methacrylate-templating and gas bubble-assisted polyvinyl alcohol-protected reduction methods, respectively. It is shown that there were good correlations of surface adsorbed oxygen species concentration and low-temperature reducibility with catalytic activity of the samples for the oxidation of CO and toluene. Among the LaMnO₃ and xAu/LaMnO₃ samples, 4.9Au/LaMnO₃ performed the best, giving the $T_{50\%}$ and $T_{90\%}$ of 61 and 91 °C for CO oxidation, and of 201 and 226 °C for toluene combustion, respectively. The apparent activation energies (29–50 and 47–62 kJ/mol) of the chain-like LaMnO₃ and xAu/LaMnO₃ samples were much smaller than those (63 and 97 kJ/mol) of the bulk LaMnO₃ sample for the oxidation of CO and toluene, respectively. We believe that the higher surface area and oxygen adspecies concentration and better low-temperature reducibility as well as the strong interaction between Au nanoparticles and chain-like LaMnO₃ support might account for the high catalytic performance of 4.9Au/LaMnO₃.

© 2013 Elsevier B.V. All rights reserved.

1. Introduction

Due to the attractive physicochemical properties, manganese-based perovskite-type oxides (AMnO₃) are important materials that have been found applications in magnetism, thermoelectronics, oxygen transportation, and catalysis [1,2]. Recently, such a kind of materials has received remarkable attention in the catalytic combustion of carbon monoxide and volatile organic compounds (VOCs) [3–6]. Since diffusion is often a problem that limits the overall performance of a bulk catalyst, making a catalyst in porous structure is expected to greatly increase the number of accessible active sites and ultimately enhance the catalytic efficiency. As demonstrated in the literature, the conventional preparation method required for generation of the pure perovskite phase at high temperatures cannot give rise to a perovskite material with high surface area. Therefore, it is highly desirable to develop an effective strategy for producing porous perovskite-type oxides. One approach to achieve this goal is the surfactant-assisted colloidal crystal-templating strategy [7]. This approach involves the

inverse replication of well-arrayed colloidal crystals into a three-dimensionally ordered macroporous (3DOM) structure [8,9], which could be disassembled into shaped building blocks. Such a disassembly extends the colloidal crystal templating method to the synthesis of cube-like and spherical silica or metal oxides and provides fine control over the particle size and morphology [10–12]. However, the strategy of using close-packed colloidal crystals as hard template and surfactant as soft template to self-assembly perovskite-type oxides with a chain-like morphology has not been reported in the literature.

In recent years, supported gold catalysts have attracted tremendous attention owing to the notable discovery by Haruta et al. [13] who observed an extraordinary activity over the supported Au nanocatalysts for low-temperature CO oxidation. It has been well established that apart from the Au particle size, the choice of support also plays a key role in the development of active Au nanocatalysts [14]. In order to obtain high-performance Au catalysts, metal oxides, such as Co₃O₄ [15], TiO₂ [16], Fe₂O₃ [17], CeO₂ [18], ZrO₂ [19], and MnO$_x$ [20], have been chosen as the support. However, these supported Au catalysts usually show insufficient stability due to the gradual loss in catalytic activity during the reaction processes. Hence, deactivation of supported Au catalysts becomes the major remaining technical hurdle to be overcome before their widespread applications. The deactivation of gold

catalysts is usually related to the accumulation of carbonate species and growth of gold particles [21,22]. The nature of the carrier is one of factors influencing the stability of gold catalysts. For example, Veith et al. found that the Au/SiO_2 catalyst exhibited much better thermal stability than the Au/TiO_2 catalyst, due to the strong binding of Au nanoparticles to defects on the silica surface [23]. Wang et al. pointed out that the Au/Mn_2O_3 catalyst possessed the best stability among the gold catalysts supported on different types of manganese oxides [20]. Considering that the perovskite-type oxides (ABO_3) exhibit good stability, highly anti-poisoning ability, and high catalytic performance, we suppose that the ABO_3-supported Au catalysts would show enhanced catalytic activity and stability. Hence, it is highly desired to establish an effective method for the controlled preparation of the Au catalysts supported on ABO_3 with porous structures and high surface areas. To the best of our knowledge, however, there have been no reports on the successful preparation of chain-like perovskite-type oxide-supported Au catalysts and their applications in catalyzing the oxidation of CO and VOCs.

Herein, we report a strategy for preparing chain-like $LaMnO_3$ and its supported Au nanocatalysts, which was based on the use of colloidal crystals as hard template to generate chain-like $LaMnO_3$ and the adopting of the gas bubble-assisted polymer protected reduction route to synthesize supported Au nanocatalysts. Briefly, high-quality colloidal crystals composed of well-arrayed poly-methyl methacrylate (PMMA) microspheres with an average size of ca. 300 nm were infiltrated with a precursor solution containing poly(ethylene glycol) (PEG). Through controlled calcination and after removal of the polymer microspheres, one could obtain an initially 3DOM structure which was then disassembled into individual chain-like particles. Subsequent incipient wetness impregnation of the chain-like $LaMnO_3$ support with the gold sol derived from the reduction of $HAuCl_4$ by sodium borohydride using polyvinyl alcohol (PVA) as protecting agent was adopted to fabricate the chain-like $LaMnO_3$-supported Au nanocatalysts. By using this novel method, high-density Au nanoparticles (NPs) could be successfully loaded onto the chain-like $LaMnO_3$ surface, and the obtained $xAu/LaMnO_3$ (x = 1.4, 3.1, and 4.9 wt%) nanocatalysts showed excellent catalytic activities and stability for the oxidation of CO and toluene.

2. Experimental

2.1. Catalyst preparation

The well-arrayed colloid crystal template PMMA microspheres with an average diameter of ca. 300 nm (Fig. S1 of the supplementary material) were synthesized according to the procedures described elsewhere [24]. In a typical fabrication of chain-like ordered macroporous $LaMnO_3$, 37.5 mmol of $La(NO_3)_3 \cdot 6H_2O$ and 37.5 mmol of $Mn(NO_3)_2$ (50 wt% aqueous solution) were dissolved in a solution of 5 mL of PEG (MW = 400 g/mol) and 5 mL of methanol at room temperature (RT) under stirring for 4 h to obtain a transparent solution. A certain amount of methanol was added to achieve a total metal concentration of 2.5 mol/L. Then, the PMMA template (2.0 g) was added to the transparent solution and soaked for 6 h. After being filtered, the mixture was dried at RT for 48 h, the obtained powders were subsequently heated in N_2 (200 mL/min) at 300 °C for 3 h, and then cooled to 50 °C in the same atmosphere, finally calcined in air (200 mL/min) at 750 °C for 4 h to remove the template, thus generating the chain-like $LaMnO_3$ sample.

The chain-like $LaMnO_3$ supported gold ($xAu/LaMnO_3$) samples were prepared via a gas bubble-assisted polymer protected reduction route using PVA (MW = 10,000 g/mol) as protecting agent and $NaBH_4$ as reducing agent. The typical preparation procedure was as follows: A desired amount of PVA (Au/PVA mass ratio = 1.5:1) was added to a $HAuCl_4$ aqueous solution (100 mg/L) at RT under vigorous stirring. A desired amount (for obtaining the theoretical Au loadings of 2, 5, and 8 wt%, respectively) of the chain-like $LaMnO_3$ support was then added to the PVA–$HAuCl_4$ mixed solution, the obtained suspension was subjected to sonication (60 kHz) for 1 min. The gas bubble-assisted stirring operation with three bubble outlets in solution was used to make the reaction homogenously. After bubbling the suspension with N_2 for 20 min, a 0.1 mol/L $NaBH_4$ aqueous solution (Au/$NaBH_4$ molar ratio = 1:5) was rapidly injected to form a dark brown suspension, i.e., the formation of Au NPs on the $LaMnO_3$ support surface, and the reaction system was further vigorously bubbled with N_2 for 2 h. The solid was collected by filtration, followed by washing with 2 L of deionized water and drying at 80 °C for 12 h, thus obtaining the $xAu/LaMnO_3$ samples. The results of inductively coupled plasma atomic emission spectroscopic (ICP-AES) investigations reveal that the real Au loading was 1.4, 3.1, and 4.9 wt% for the Au-loaded samples, respectively. For comparison purposes, the bulk $LaMnO_3$ sample was prepared via the citric acid-complexing route [25]. The 4.6 wt% Au/bulk $LaMnO_3$ sample was also prepared using the method similar to that for the preparation of the $xAu/LaMnO_3$ samples.

All of the above steps were carried out by covering all of the containers with a layer of aluminum foil. All of the chemicals (A.R. in purity) were purchased from Sinopharm Chemical Reagent Beijing Company and used without further purification.

2.2. Catalyst characterization

X-ray diffraction (XRD) patterns of the samples were recorded on a Bruker D8 Advance diffractometer with Cu Kα radiation and nickel filter (λ = 0.15406 nm). Thermogravimetric analysis (TGA) and differential scanning calorimetric (DSC) analysis of the uncalcined samples were conducted over a SDT Q600 (TA) apparatus. Elemental analysis with respect to Au loading was performed using the ICP-AES technique on a Thermo Electron IRIS Intrepid ER/S spectrometer. Fourier transform infrared (FT-IR) spectra of the samples (1 wt% sample + 99 wt% KBr) were obtained in the 400–4000 cm^{-1} range with a resolution of 0.4 cm^{-1} on a Bruker Vertex 70 spectrometer. The samples were dissolved in a mixture of concentrated HCl and HNO_3 with volumetric ratio of 3/1 prior to the analysis. BET (Brunauer–Emmett–Teller) surface areas of the samples were measured via N_2 adsorption at −196 °C on a Micromeritics ASAP 2020 analyzer with the samples outgassed at 300 °C for 2.5 h under vacuum before measurement. The scanning electron microscopic (SEM) images of the samples were recorded on a Gemini Zeiss Supra 55 apparatus (operating at 10 kV). Transmission electron microscopic (TEM) images of the samples were obtained using the JEOL-2010 equipment (operating at 200 kV). X-ray photoelectron spectroscopy (XPS, VG CLAM 4 MCD analyzer) was used to determine the La 3d, Mn 2p, O 1 s, Au 4f and C 1 s binding energies (BEs) of surface species using Mg Kα ($h\nu$ = 1253.6 eV) as the excitation source. Hydrogen temperature-programmed reduction (H_2-TPR) experiments were carried out on a chemical adsorption analyzer (Autochem II 2920, Micromeritics). Before TPR measurement, ca. 0.02 g of catalyst (40–60 mesh) was loaded to a quartz fixed-bed U-shaped microreactor (i.d. = 4 mm) and pretreated in an O_2 flow of 30 mL/min at 500 °C for 1 h, so that the adsorbed water and carbon dioxide could be totally removed and no reduction of the catalysts took place. After being cooled at the same atmosphere to RT and then purged with a helium flow of 30 mL/min for 15 min, the pretreated sample was finally exposed to a flow (50 mL/min) of 5% H_2–95% Ar (v/v) mixture and heated from RT to 850 °C at a ramp of 10 °C/min. The alteration in H_2 concentration of the effluent was monitored on-line by the chemical adsorption analyzer. The
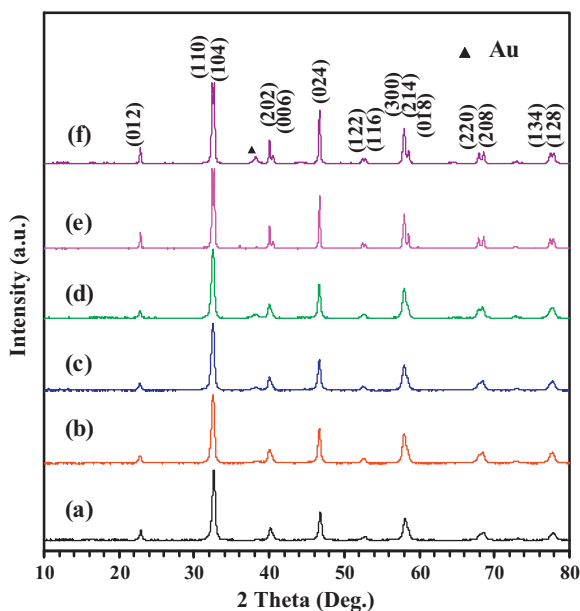
Fig. 1. XRD patterns of (a) chain-like LaMnO$_3$, (b) 1.4Au/LaMnO$_3$, (c) 3.1Au/LaMnO$_3$, (d) 4.9Au/LaMnO$_3$, (e) LaMnO$_3$-bulk, and (f) 4.6Au/bulk LaMnO$_3$.

reduction band was calibrated against that of the complete reduction of a standard CuO sample (Aldrich, 99.995%).

2.3. Catalytic evaluation

The catalytic activity was evaluated with the sample charged in a continuous flow fixed-bed quartz microreactor (i.d. = 4 mm). To minimize the effect of hot spots, the sample (50 mg, 40–60 mesh) was diluted with 0.25 g quartz sands (40–60 mesh). For CO oxidation, the reactant feed was 1% CO + 20% O$_2$ + N$_2$ (balance), and the total flow rate was 16.7 mL/min, giving a space velocity (SV) of ca. 20,000 mL/(g h). Prior to the test, the sample was treated in O$_2$ (30 mL/min) at 250 °C for 1 h. After being cooled at the same atmosphere to a given temperature, the reactant gas mixture was switched to the microreactor for activity measurements. Reactants and products were analyzed on-line by a gas chromatograph (GC-14C, Shimadzu) equipped with a thermal conductivity detector (TCD), using a 13× column. For toluene oxidation, the total flow rate of the reactant mixture (1000 ppm toluene + 40 vol% O$_2$ + N$_2$ (balance)) was 16.7 mL/min, giving a toluene/O$_2$ molar ratio of 1/400 and a SV of ca. 20,000 mL/(g h). The 1000-ppm toluene was generated by passing a N$_2$ flow through a bottle containing pure toluene chilled in an ice-water isothermal bath. Reactants and products were analyzed on-line by a gas chromatograph (GC-2010, Shimadzu) equipped with a flame ionization detector (FID), using a stabilwax@-DA column (30 m in length) for permanent gas separation. For the kinetic studies, the turnover frequencies TOF$_{Au}$ (or TOF$_{Mn}$) and reaction rates (μmol/(g$_{Au}$ s)) were calculated according to the single surface Au site (or molar amount of Mn) and the Au weight in the xAu/LaMnO$_3$ samples, respectively. The amounts of Au sites were estimated according to the procedure reported in the literature [26] and the assumption that the Au particles showed a spherical or hemispherical shape (as confirmed by the high-resolution TEM observations).

3. Results and discussion

3.1. Crystal phase composition

Fig. 1 shows the XRD patterns of the as-prepared LaMnO$_3$ and supported gold samples with different Au loadings. It is observed

that compared to the XRD pattern of the chain-like LaMnO$_3$ support, the loading of Au did not lead to any changes in perovskite structure. The XRD patterns clearly reveal that the crystal structures of all of the samples could be indexed to the rhombohedral LaMnO$_3$ perovskite structure (JCPDS PDF# 82-1152); and the calculated grain sizes of chain-like LaMnO$_3$ and bulk LaMnO$_3$ were ca. 33 and 118 nm, respectively. Weak diffraction of Au (1 1 1) was detected at 2θ = 38.5°. The results confirm the formation of cubic Au NPs (JCPDS PDF# 04-0784) on the LaMnO$_3$ surface. The TGA/DSC results (Fig. S2 of the supplementary material) demonstrate that the calcination conditions were appropriate for the generation of single-phase perovskite structure. The FT-IR results (Fig. S3 of the supplementary material) indicate that all of the organics employed in the preparation processes were removed completely from the surface of xAu/LaMnO$_3$.

### 3.2. Morphology, pore structure, and surface area

Fig. 2 shows the SEM and TEM images as well as the SAED patterns of the samples. It can be observed from Fig. 2a and b that there were bundles of well-defined chain-like nanoentities with a uniform diameter in the LaMnO$_3$ sample. The average pore size was approximately 50 nm, and the average wall thickness was about 23 nm. It is clearly seen from Fig. 2c, d, f, h, j and k that the individual chain-like nanoentity consisted of continuous macropores stacked along the chain axis, in good agreement with the SEM observations. The uniform Au NPs were well dispersed on the LaMnO$_3$ support surface. The Au particle sizes of the 1.4Au/LaMnO$_3$, 3.1Au/LaMnO$_3$, and 4.9Au/LaMnO$_3$ samples were in the ranges of 2–4, 2–5, and 2–5 nm, respectively. From the high-resolution TEM (HRTEM) image of chain-like LaMnO$_3$, the intraplanar spacing was measured to be 0.16 nm, in good consistence with that of the (2 1 4) crystal plane of the standard LaMnO$_3$ sample (JCPDS PDF# 82-1152). The observation of multiple bright electron diffraction rings in the inset SAED patterns of the LaMnO$_3$ and xAu/LaMnO$_3$ samples suggests the formation of polycrystalline structure. The HRTEM images of the xAu/LaMnO$_3$ samples also reveal that the lattice spacing of the Au NPs was 0.14–0.15 nm, rather close to that of the (2 2 0) crystal plane of the standard Au sample (JCPDS PDF# 04-0784). The possible formation mechanisms of the chain-like LaMnO$_3$ and xAu/LaMnO$_3$ samples are described in the supplementary material (Figs. S4 and S5).

Fig. 3 shows the N$_2$ adsorption–desorption isotherms and pore-size distributions of the samples. From Fig. 3A, one can see that all of the samples displayed a N$_2$ adsorption-desorption isotherm characteristic of a combination of macropore and mesopore structures. The hysteresis loops in the low and high relative pressure ranges of the Au-loaded samples were slightly different from that of the chain-like LaMnO$_3$ sample, indicative of the discrepancy in pore-size distribution (Fig. 3B). Table 1 summarizes the textural parameters of the LaMnO$_3$ and xAu/LaMnO$_3$ samples. The bulk LaMnO$_3$ and 4.6Au/LaMnO$_3$ samples exhibited a low surface area (7.3–7.8 m^2/g), whereas the chain-like LaMnO$_3$ and xAu/LaMnO$_3$ samples possessed much higher surface areas (29.8–32.7 m^2/g). The pore volumes of these porous materials were in the range of 0.084–0.092 cm^3/g.

3.3. Surface composition, metal oxidation state, and oxygen species

Fig. 4 shows the Mn 2p$_{3/2}$, O 1s, and Au 4f XPS spectra of the LaMnO$_3$ and xAu/LaMnO$_3$ samples. It can be observed from Fig. 4A that the asymmetrical Mn 2p$_{3/2}$ XPS spectrum of each sample could be decomposed to three components at BE = 641.4, 642.8, and 644.8 eV, assignable to the surface Mn^{3+} and Mn^{4+} species and satellite of Mn^{3+} species [27], respectively. As summarized in
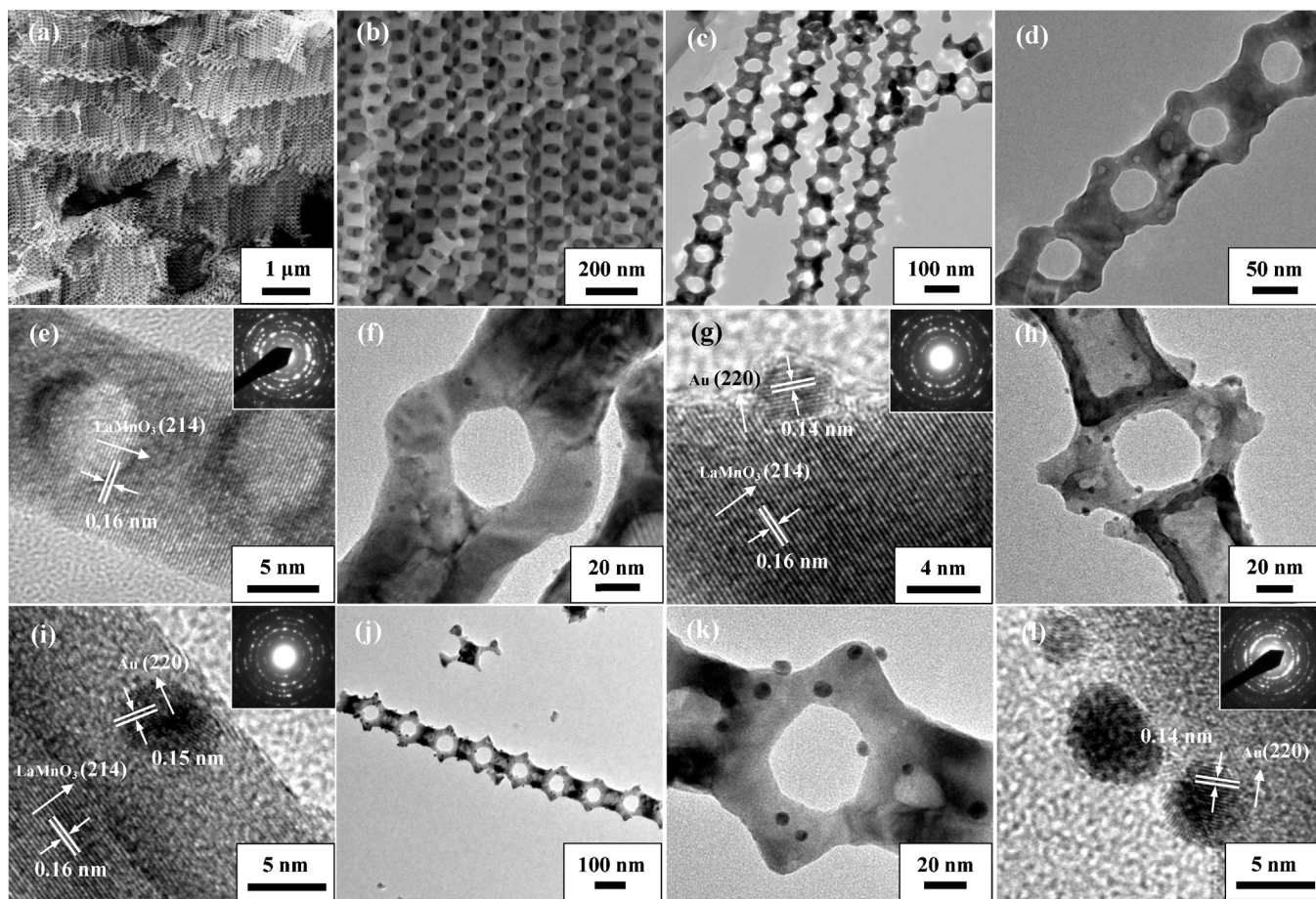
Fig. 2. (a, b) SEM and (c–l) TEM images and SAED patterns (insets) of (a–e) chain-like $LaMnO_3$, (f, g) 1.4Au/$LaMnO_3$, (h, i) 3.1Au/$LaMnO_3$, and (j–l) 4.9Au/$LaMnO_3$.

Table 2, the surface Mn^{4+}/Mn^{3+} molar ratio decreased from chain-like $LaMnO_3$ (1.32) to 4.9Au/$LaMnO_3$ (0.79). For each sample, the O 1s spectrum (Fig. 4B) could be decomposed to three components at BE = 529.1, 531.1, and 533.4 eV, attributable to the surface lattice oxygen (O_{latt}), adsorbed oxygen (O_{ads}, e.g. O_2^-, O_2^{2-} or O^-), and carbonate species [28,29], respectively. The surface O_{ads}/O_{latt} molar ratio increased remarkably after the loading of Au on the

chain-like $LaMnO_3$ support (Table 2). The rise in surface active oxygen species concentration would give rise to enhanced catalytic performance of xAu/$LaMnO_3$ for the total oxidation of CO and toluene [28,30]. Deconvolution of the Au XPS spectra (Fig. 4C) indicates that both metallic (in majority) and ionic (in minority) gold species were present in the supported Au samples. The Au 4f spectrum of each xAu/$LaMnO_3$ sample is featured by the signals
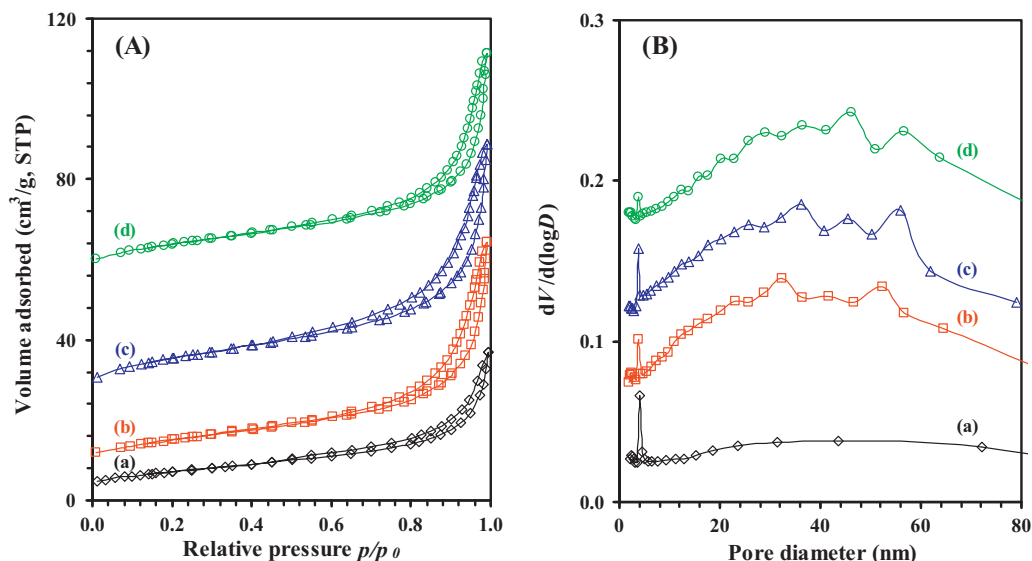
Fig. 3. (A) Nitrogen adsorption–desorption isotherms and (B) pore-size distributions of (a) chain-like $LaMnO_3$, (b) 1.4Au/$LaMnO_3$, (c) 3.1Au/$LaMnO_3$, and (d) 4.9Au/$LaMnO_3$.

Table 1

BET surface areas, pore volumes, average crystallite sizes, Au particle sizes, and real Au contents of the LaMnO$_3$, 4.6Au/bulk LaMnO$_3$, and xAu/LaMnO$_3$ samples.

Sample	BET surface area (m^2/g)	Pore volume (cm^3/g)	D_{LaMnO3} (nm)[a]	Au particle size (nm)[b]	Au content (wt%)[c]
LaMnO$_3$-bulk	7.3	–	118	–	–
Chain-like LaMnO$_3$	31.5	0.084	33	–	–
1.4Au/LaMnO$_3$	30.6	0.086	35	2–4	1.4
3.1Au/LaMnO$_3$	29.8	0.092	34	2–5	3.1
4.9Au/LaMnO$_3$	32.7	0.088	33	2–5	4.9
4.6Au/bulk LaMnO$_3$	7.8	–	112	4–10	4.6

[a] Data determined based on the XRD results according to the Scherrer equation using the FWHM of the (1 1 0) line of LaMnO$_3$.
[b] Estimated according to the TEM images.
[c] Determined by the ICP-AES technique.
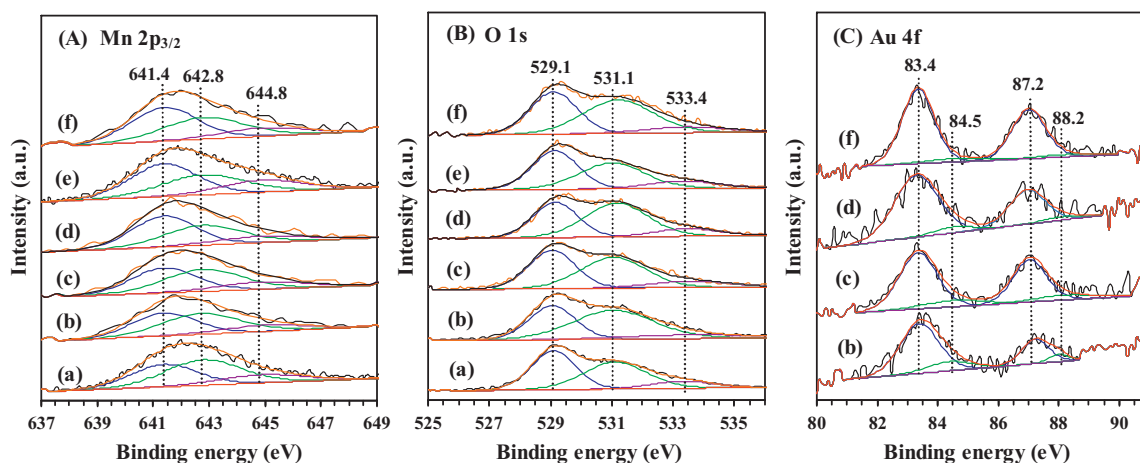
Fig. 4. (A) Mn 2p$_{3/2}$, (B) O 1s, and (C) Au 4f XPS spectra of (a) chain-like LaMnO$_3$, (b) 1.4Au/LaMnO$_3$, (c) 3.1Au/LaMnO$_3$, (d) 4.9Au/LaMnO$_3$, (e) LaMnO$_3$-bulk, and (f) 4.6Au/bulk LaMnO$_3$.

at BE = 83.4, 87.2, 84.5, and 88.2 eV, the former two were due to the surface Au^0 whereas the latter two were due to the surface Au$^{\delta+}$ [31,32]. Several previous studies give strong evidence that CO is only weakly adsorbed on zero-valent gold and more strongly adsorbed on cationic gold. It is suggested that the cationic gold sites may be kinetically more significant than the zero-valent gold sites under practical reaction conditions [33,34]. With the rise in Au loading, the gold particle size increased slightly, but the Au$^{\delta+}$/Au^0 molar ratio decreased. Similar results have also been reported by Wei et al. [31].

As a general rule, when a metal phase is deposited on a support surface, a strong metal–support interaction can occur. After the loading of gold, the rise in Mn^{3+} content of the xAu/LaMnO$_3$ samples indicates that a strong interaction existed between Au and LaMnO$_3$, a result due to the electron transfer from Au^0 to Mn^{4+} in the LaMnO$_3$ support. In other words, the Au atoms (Au^0 → Au$^{\delta+}$) can be oxidized by the surface Mn atoms (Mn^{4+} → Mn^{3+}) even though there is no direct Au–Mn bonding. Furthermore, the change in low-temperature reducibility of the LaMnO$_3$ and xAu/LaMnO$_3$ samples (shown below) also suggests the presence of a strong interaction between Au and LaMnO$_3$.

3.4. Reducibility

TPR experiments were carried out to investigate the redox properties of the LaMnO$_3$ sample and its supported gold catalysts, and the results are shown in Fig. 5A. The chain-like LaMnO$_3$ sample exhibited stepwise reduction [35,36]: the reduction peak at 292 °C was attributable to the reduction of Mn^{4+} to Mn^{3+} as well as the removal of over-stoichiometric oxygen and oxygen adspecies, the shoulder at 391 °C was assignable to the single-electron reduction of Mn^{3+} located in a coordination-unsaturated microenvironment, whereas the reduction peak above 600 °C was due to the reduction

of the left Mn^{3+} to Mn^{2+}. The two reduction temperatures (348 and 830 °C) of the bulk LaMnO$_3$ sample were much higher than those (292 and 691 °C) of the porous counterpart, indicating that formation of a chain-like structure could facilitate the reduction of LaMnO$_3$. When Au was loaded onto the LaMnO$_3$ surface, all of the reduction peaks shifted to lower temperatures. The result suggests the presence of a strong interaction between Au NPs and LaMnO$_3$ support in xAu/LaMnO$_3$. The first reduction peak was due to the reduction of the chemically adsorbed oxygen species on the highly dispersed Au NPs (i.e., from Au–O$_x$ to Au) or the interface between Au NPs and LaMnO$_3$ support (i.e., from Mn–O$_x$–Au to Au), which might be related to the weakening of the Mn–O bond induced by Au atom [20,30]. Through quantitative analysis of the H$_2$-TPR profiles, one can obtain the H$_2$ consumption of each sample, as summarized in Table 2. The total H$_2$ consumption of the LaMnO$_3$ and xAu/LaMnO$_3$ samples was in the range of 3.14–3.59 mmol/g. The reduction of LaMnO$_{3+\delta}$ usually proceeds via the sequence of Mn^{4+} → Mn^{3+} → Mn^{2+}. If manganese ions in LaMnO$_{3+\delta}$ were Mn^{4+} and Mn^{3+} and reduced to Mn^{2+}, the H$_2$ consumption would be 4.14 and 2.07 mmol/g, respectively. It has been reported that there is 35% Mn^{4+} and 65% Mn^{3+} (which leads to the presence of nonstoichiometric oxygen in LaMnO$_{3+\delta}$), corresponding to a H$_2$ consumption of 2.80 mmol/g if Mn^{4+} and Mn^{3+} are reduced to Mn^{2+} [37,38]. In our case, the total H$_2$ consumption of chain-like LaMnO$_{3+\delta}$ was 3.59 mmol/g, which was higher than the above value. The discrepancy in H$_2$ consumption of LaMnO$_{3+\delta}$ and chain-like LaMnO$_{3+\delta}$ was due to the removal of nonstoichiometric oxygen in LaMnO$_{3+\delta}$ and adsorbed oxygen species on the chain-like LaMnO$_{3+\delta}$ surface during the reduction processes. Furthermore, the reduction of a small amount of AuO$_x$ in xAu/LaMnO$_3$ could contribute to the increase in H$_2$ consumption. From Table 2, one can clearly see that the low-temperature (<550 °C) H$_2$ consumption increased
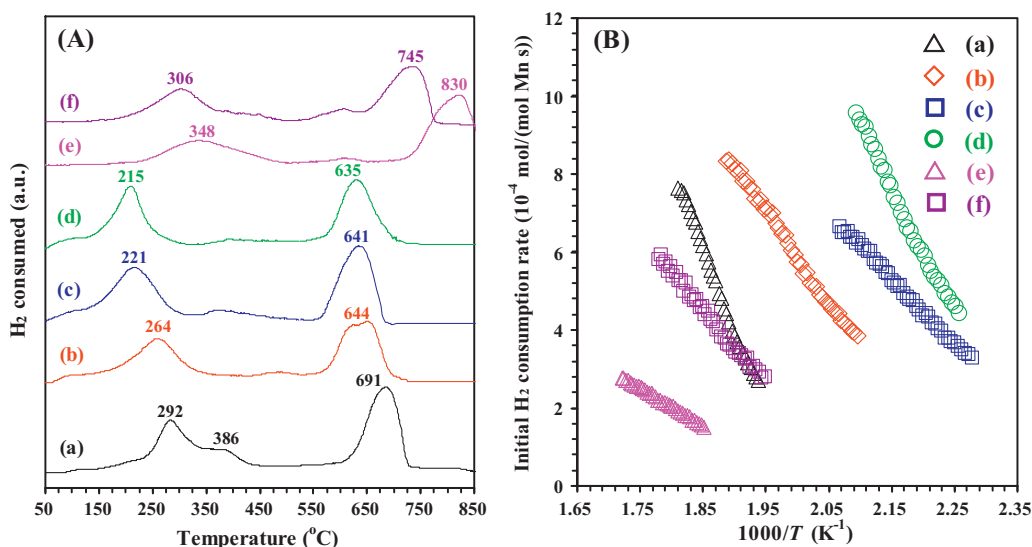
Fig. 5. (A) H_2-TPR profiles and (B) initial H_2 consumption rate as a function of inverse temperature of (a) chain-like $LaMnO_3$, (b) 1.4Au/$LaMnO_3$, (c) 3.1Au/$LaMnO_3$, (d) 4.9Au/$LaMnO_3$, (e) $LaMnO_3$-bulk, and (f) 4.6Au/bulk $LaMnO_3$.

in the order of $LaMnO_3$-bulk < 4.6Au/bulk $LaMnO_3$ < chain-like $LaMnO_3$ < 1.4Au/$LaMnO_3$ < 3.1Au/$LaMnO_3$ < 4.9Au/$LaMnO_3$. It has been generally accepted that the low-temperature reducibility of a catalyst can be conveniently evaluated by using the initial H_2 consumption rate [39,40]. The initial H_2 consumption rate was calculated according to the H_2 amount consumed per mole of Mn/s, which corresponded to the initial 25% area of the first reduction peak where no phase transformation of the catalyst occurred. Fig. 5B shows the initial H_2 consumption rate as a function of inverse temperature of the $LaMnO_3$ and xAu/$LaMnO_3$ samples. It is clearly seen that the initial H_2 consumption rate decreased in the order of $LaMnO_3$-bulk < 4.6Au/bulk $LaMnO_3$ < chain-like $LaMnO_3$ < 1.4Au/$LaMnO_3$ < 3.1Au/$LaMnO_3$ < 4.9Au/$LaMnO_3$. Such trends in low-temperature reducibility were in good accordance with the sequence of catalytic performance shown below.

3.5. Catalytic performance

Fig. 6A and B shows the catalytic performance of the $LaMnO_3$ and xAu/$LaMnO_3$ samples for the oxidation of CO and toluene, respectively. It can be clearly observed that the chain-like $LaMnO_3$ and xAu/$LaMnO_3$ samples performed much better than the bulk

$LaMnO_3$ and 4.6Au/bulk $LaMnO_3$ samples, especially for the oxidation of CO. This result suggests that the porous materials outperformed the nonporous bulk counterparts for CO and toluene oxidation. In addition, the change trend in CO or toluene conversion versus temperature was quite similar to that in CO or toluene consumption rate versus temperature (Fig. S6 of the supplementary material). It should be pointed out that toluene was completely oxidized to CO_2 and H_2O over the $LaMnO_3$ and xAu/$LaMnO_3$ catalysts, and there was no detection of incomplete oxidation products, as substantiated by the good carbon balance (ca. 99.5%) in each run. According to the Weisz-Prater criterion, when the effectiveness factor $\eta \geq 0.95$ and reaction order $n = 1$, the dimensionless Weisz-Prater parameter (ϕ_{WP}) value is less than 0.3, which can be considered a sufficient condition for the absence of significant pore diffusion limitations [41]. At CO and toluene conversion ≤ 20%, we carried out the Weisz-Prater analysis, and calculated the ϕ_{WP} values, which were much less than 0.3. The absence of internal mass diffusion transport resistance was checked by the Weisz-Prater Criterion (N_{W-P}) [42] and the calculation method is described in the supplementary material. It is found that the N_{W-P} value was 6.53×10^{-3} for CO oxidation and 6.98×10^{-3} for toluene oxidation, which were much less than 0.3. The heat transfer issue can
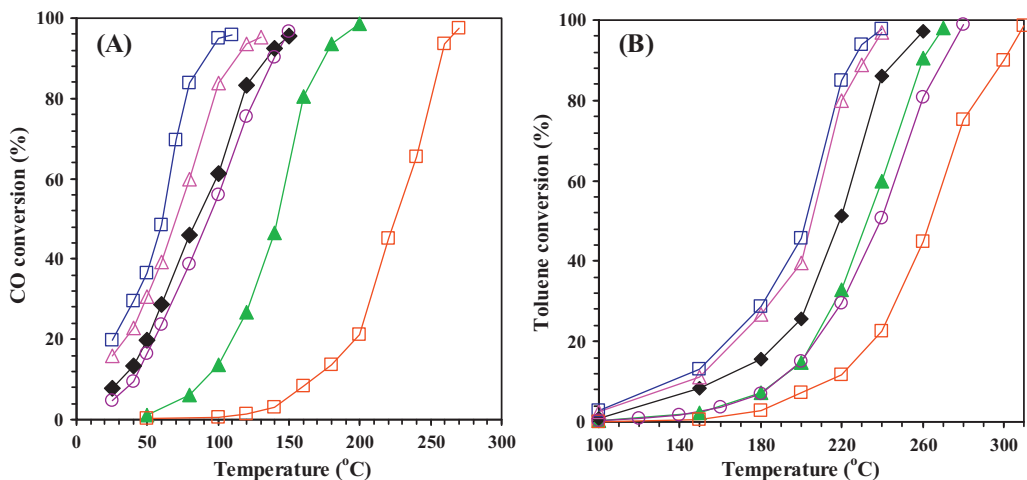
Fig. 6. (A) CO conversion and (B) toluene conversion as a function of reaction temperature over (□) $LaMnO_3$-bulk, (▲) chain-like $LaMnO_3$, (♦) 1.4Au/$LaMnO_3$, (△) 3.1Au/$LaMnO_3$, (□) 4.9Au/$LaMnO_3$, and (△) 4.6Au/bulk $LaMnO_3$.

Table 2
Surface element compositions, H_2 consumption and catalytic activities of the $LaMnO_3$, $4.6Au/bulk$ $LaMnO_3$, and $xAu/LaMnO_3$ samples.

Catalyst	Mn^{4+}/Mn^{3+} molar ratio	Au^{3+}/Au^0 molar ratio	O_{ads}/O_{latt} molar ratio	H_2 consumption (mmol/g)[a]		CO oxidation activity and apparent activation energy				Toluene oxidation activity and apparent activation energy			
				<550 °C	≥550 °C	$T_{10\%}$ (°C)	$T_{50\%}$ (°C)	$T_{90\%}$ (°C)	E_a (kJ/mol)	$T_{10\%}$ (°C)	$T_{50\%}$ (°C)	$T_{90\%}$ (°C)	E_a (kJ/mol)
$LaMnO_3$–bulk	0.80	–	0.87	0.97	2.17	166	225	259	63	211	263	300	97
Chain-like $LaMnO_3$	1.32	–	1.08	1.80	1.79	89	137	179	50	188	232	260	62
$1.4Au/LaMnO_3$	1.12	0.21	1.21	1.82	1.70	31	86	134	37	158	219	248	52
$3.1Au/LaMnO_3$	1.02	0.18	1.43	1.86	1.72	–	72	117	29	147	205	231	48
$4.9Au/LaMnO_3$	0.79	0.09	1.57	1.92	1.60	–	61	91	30	138	201	226	47
$4.6Au/bulk$ $LaMnO_3$	0.73	0.08	1.20	1.40	1.78	42	92	140	43	189	240	271	52
used $4.9Au/LaMnO_3$[b]	0.83	0.08	1.56	–	–	–	–	–	–	–	–	–	–
used $4.9Au/LaMnO_3$[c]	0.80	0.08	1.46	–	–	–	–	–	–	–	–	–	–

[a] The data were estimated by quantitatively analyzing the H_2-TPR profiles.
[b] The $4.9Au/LaMnO_3$ sample after 100 h of on-stream reaction for CO oxidation under the conditions of CO concentration = 1 vol%, CO/O_2 molar ratio = 1/20, SV = 20,000 mL/(g h), and temperature = 100 °C.
[c] The $4.9Au/LaMnO_3$ sample after 100 h of on-stream reaction for toluene oxidation under the conditions of toluene concentration = 1000 ppm, toluene/O_2 molar ratio = 1/400, SV = 20,000 mL/(g h), and temperature = 220 °C.

be checked by using the Koros–Nowak Test [43]. The calculated results (see Table S1 of the supplementary material) indicate that the turnover frequency TOF_{Au} values over the $xAu/LaMnO_3$ catalysts either for CO oxidation or for toluene oxidation were basically the same. Therefore, no significant heat and mass transfer problems were present in our catalytic system.

It is convenient to compare the catalytic activities of the samples by adopting the reaction temperatures $T_{10\%}$, $T_{50\%}$, and $T_{90\%}$ (corresponding to the CO or toluene conversion = 10, 50, and 90%), as summarized in Table 2. It is found that the chain-like $LaMnO_3$ catalyst showed better performance than the $LaMnO_3$-bulk catalyst, with the $4.9Au/LaMnO_3$ sample performing the best. Over the $4.9Au/LaMnO_3$ catalyst, the $T_{50\%}$ and $T_{90\%}$ values were 61 and 91 °C for CO oxidation, and 201 and 226 °C for toluene combustion, respectively; over the $4.6Au/bulk$ $LaMnO_3$ catalyst, the $T_{50\%}$ and $T_{90\%}$ values were 92 and 140 °C for CO oxidation, and 240 and 271 °C for toluene combustion, respectively. According to the activity data and mole of Mn in the $LaMnO_3$ and $xAu/LaMnO_3$ catalysts, we calculated the turnover frequency (TOF_{Au} or TOF_{Mn}) and reaction rates (μmol/(g_{Au} s)) according to the single surface Au site (or mole of Mn) and the Au weight in the $xAu/LaMnO_3$ samples, respectively. The TOF_{Au} was calculated according to the number of CO or toluene molecules converted by single surface Au site/s. The dispersion of gold was estimated according to the reported procedure [26] and the assumption that the Au particles displayed a spherical or hemispherical shape (as confirmed by our high-resolution TEM images (Fig. 2f, h, k, and l) of the samples). Table 3 summarizes the TOF_{Au} and TOF_{Mn} of the samples. Compared to the nonporous $LaMnO_3$-bulk and $4.6Au/LaMnO_3$ sample at the same temperature, the TOF_{Mn} values of the chain-like porous $LaMnO_3$ and $xAu/LaMnO_3$ samples were much higher. For example, the TOF_{Mn} value (0.55×10^{-3} s^{-1}) of $4.9Au/LaMnO_3$ was seven times as much as that (0.075×10^{-3} s^{-1}) of chain-like $LaMnO_3$ for CO oxidation at 100 °C; the TOF_{Mn} value (0.027×10^{-3} s^{-1}) of $4.9Au/LaMnO_3$ was approximately three times as much as that (0.0082×10^{-3} s^{-1}) of chain-like $LaMnO_3$ for toluene combustion at 200 °C. This result indicates that there was a strong interaction between the metal (Au) and the support ($LaMnO_3$), which gave rise to an enhanced catalytic performance of $xAu/LaMnO_3$ for CO and toluene oxidation. From Table 3, one can also observe that the TOF_{Au} values (2.2–2.4 for CO oxidation at 50 °C and 2.8–3.1 for toluene oxidation at 200 °C) of the $xAu/LaMnO_3$ samples were much higher than that (1.6 for CO oxidation at 50 °C and 1.5 for toluene oxidation at 200 °C) of the $4.6Au/bulk$ $LaMnO_3$ sample. The reaction rate (17.0–32.4 μmol/(g_{Au} s)) for CO oxidation at 50 °C over $xAu/LaMnO_3$ was higher than that (14.2 μmol/(g_{Au} s)) over 3.6 wt% $Au/LaCoO_3$ [44], but inferior to that (74.3 μmol/(g_{Au} s)) over 8 wt% Au/MnO_2 [20]. In addition, the catalytic activity of a supported Au catalyst is quite sensitive to the particle size, which is induced by the Au particle size effect [45]. In the present study, the higher activity of the $xAu/porous$ $LaMnO_3$ catalysts could be not only due to the better dispersion of the gold, but also the smaller size (2–5 nm) of Au particles as compared to the $4.6Au/bulk$ $LaMnO_3$ catalyst.

Fig. 7 shows the catalytic activity of $4.9Au/LaMnO_3$ for CO oxidation at 100 °C and for toluene combustion at 220 °C within 100 h of on-stream reaction. No significant loss in catalytic activity was observed both for CO and toluene oxidation. Furthermore, the XRD pattern (Fig. S7 of the supplementary material) and Mn $2p_{3/2}$ and O 1s XPS spectrum (Fig. S8 of the supplementary material) of the used catalyst was rather similar to those of the fresh sample. The surface Mn^{4+}/Mn^{3+} (0.80–0.83) and O_{ads}/O_{latt} (1.46–1.56) molar ratios of the used sample were also similar to those (0.79 and 1.57, respectively) of the fresh sample (Table 2). These results demonstrate that the $4.9Au/LaMnO_3$ sample was durable catalytically.

Table 3
The reaction rates and TOF values for CO and toluene oxidation over the $LaMnO_3$, 4.6Au/bulk $LaMnO_3$, and xAu/$LaMnO_3$ samples at different temperatures.

Sample	CO oxidation at 50 °C			CO oxidation at 100 °C			Toluene combustion at 200 °C		
	Reaction rate (μmol/(g_{Au} s))	TOF_{Au} ($\times 10^{-2}$ s^{-1})	TOF_{Mn} ($\times 10^{-3}$ s^{-1})	Reaction rate (μmol/(g_{Au} s))	TOF_{Au} ($\times 10^{-2}$ s^{-1})	TOF_{Mn} ($\times 10^{-3}$ s^{-1})	Reaction rate (μmol/(g_{Au} s))	TOF_{Au} ($\times 10^{-3}$ s^{-1})	TOF_{Mn} ($\times 10^{-3}$ s^{-1})
$LaMnO_3$-bulk	–	–	–	–	–	0.0024	–	–	0.0040
Chain-like $LaMnO_3$	–	–	0.0069	–	–	0.075	–	–	0.0082
1.4Au/$LaMnO_3$	32.4	2.2	0.11	99.7	6.7	0.34	4.2	2.8	0.014
3.1Au/$LaMnO_3$	22.5	2.4	0.17	61.6	6.6	0.48	2.9	3.1	0.023
4.9Au/$LaMnO_3$	17.0	2.3	0.21	44.2	6.0	0.55	2.1	2.8	0.027
4.6Au/bulk $LaMnO_3$	8.1	1.6	0.095	27.7	5.6	0.33	0.74	1.5	0.0087

It is well known that catalytic activity of a solid oxide is associated with several factors, such as defective structure, oxygen adspecies concentration, reducibility, surface area, and morphology. For the combustion of organics, the catalyst with a higher surface area would show a better catalytic activity [46,47]. The surface areas of the chain-like $LaMnO_3$ and xAu/$LaMnO_3$ samples were much higher than that of the bulk $LaMnO_3$ and 4.6Au/bulk $LaMnO_3$ samples, causing the former to perform much better for the oxidation of CO and toluene. This result indicates that surface area was an important factor influencing the catalytic performance. Usually, a higher structural defect (e.g., oxygen nonstoichiometry) density is beneficial for the activation of oxygen molecules to active oxygen adspecies, and a stronger reducibility renders the catalyst to show better catalytic performance [48]. As revealed by the XPS and H_2-TPR investigations, the oxygen adspecies concentration relevant to the surface oxygen nonstoichiometry and low-temperature reducibility were related to the catalytic activity of the xAu/$LaMnO_3$ samples. It has been generally accepted that the sites active for the total oxidation of toluene differ from those associated with CO oxidation. The active sites for the oxidation of toluene may not merely be the sites at the interface between the gold NPs and the $LaMnO_3$ support. The mechanism of VOC oxidation over the ceria-supported gold and other reducible metal oxide catalysts [49–51] has been proposed. These authors believed that the oxidation of VOCs over these catalysts would follow the Mars and van Krevelen mechanism [52]. The key steps of this mechanism are the supply of active oxygen species by the readily reducible oxide and its re-oxidation by gas-phase oxygen molecules. $LaMnO_3$ possesses an ability to undergo rapid redox cycles ($Mn^{3+} \Leftrightarrow Mn^{4+}$). In this way, $LaMnO_3$ can control and maintain the adequate oxidation state of gold active sites, hence leading to an enhancement in catalytic activity. There might be a direct relationship between reducibility and catalytic performance of a material. The high catalytic performance of xAu/$LaMnO_3$ was related to their stronger low-temperature reducibility. On the other hand, hydrocarbons can interact with Au surfaces via its π bond [53]. The activation of oxygen is a difficult step on the gold surface [54]. However, a high dispersion of gold on the $LaMnO_3$ surface favors formation of a large number of catalytic sites for the activation of hydrocarbons, thus attaining a high catalytic activity. The presence of chain-like pores in the $LaMnO_3$ support facilitated generation of xAu/$LaMnO_3$ with a high Au dispersion and for the adsorption and diffusion of reactant molecules. In addition, the oxidation state of gold would also play a key role in the catalytic combustion of toluene. For example, the oxidation of toluene over gold/iron oxide decreased greatly when the oxidized gold species in the catalyst disappeared [55]. Wang and Ro [56] observed a higher activity of oxidized gold than that of metallic gold for the total oxidation of methanol. Waters et al. [57] claimed that the gold with higher oxidation states could promote the catalytic combustion of methane. Casaletto et al. [58] pointed out that the higher catalytic performance for CO oxidation over Au/CeO_2 with respect to Au/SiO_2 was ascribed to a better stabilization of the Au$^{\delta+}$ species by cerium ions. The above results and discussion demonstrate that the presence of Au with an oxidized state was beneficial for enhancement in catalytic activity. For a supported metal catalyst, the metal–support interaction would have an important role to play in determining its physicochemical property. A large number of works on the supported Au catalysts demonstrate that the metal–support interaction is beneficial for improvement in catalytic activity (e.g., [56–58,17,59,60]). In our present studies, the changes in surface Mn^{4+}/Mn^{3+} molar ratio and the low-temperature reducibility induced by the loading of Au suggest the presence of a strong interaction between Au NPs and chain-like $LaMnO_3$ support, which favored the enhancement in catalytic performance. Therefore, we conclude that the high catalytic performance of the 4.9Au/$LaMnO_3$ sample for the oxidation of CO and toluene was mainly related to its high surface area and oxygen adspecies concentration, good low-temperature reducibility, and strong interaction between Au and $LaMnO_3$.

3.6. Activation energy

In the past years, there have been reports on the kinetics of catalytic oxidation of VOC and CO. For example, Wong et al. claimed that the oxidation of butyl acetate over the AgZSM-5 catalyst was first-order toward butyl acetate concentration and zero toward oxygen concentration [61]; by assuming a first-order kinetics with respect to toluene and a zero-order kinetics with respect to oxygen, Alifanti et al. obtained good linear Arrhenius plots for the oxidation of toluene over ceria–zirconia-supported $LaCoO_3$ catalysts [62]. Jia et al. have proposed that the oxidation of CO over the CuO/$Ce_{1-x}Cu_xO_{2-\delta}$ catalyst was first-order toward CO concentration and zero toward oxygen
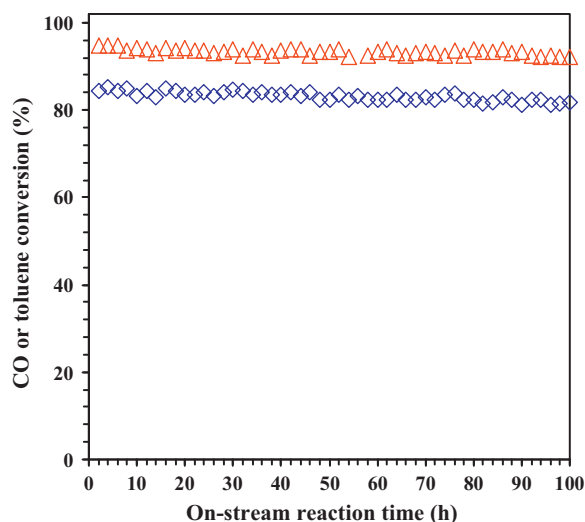
Fig. 7. Catalytic activity versus on-stream reaction time over the 4.9Au/$LaMnO_3$ catalyst for the oxidation of ($\bigcirc$) CO at 100 °C and ($\Diamond$) toluene at 220 °C.
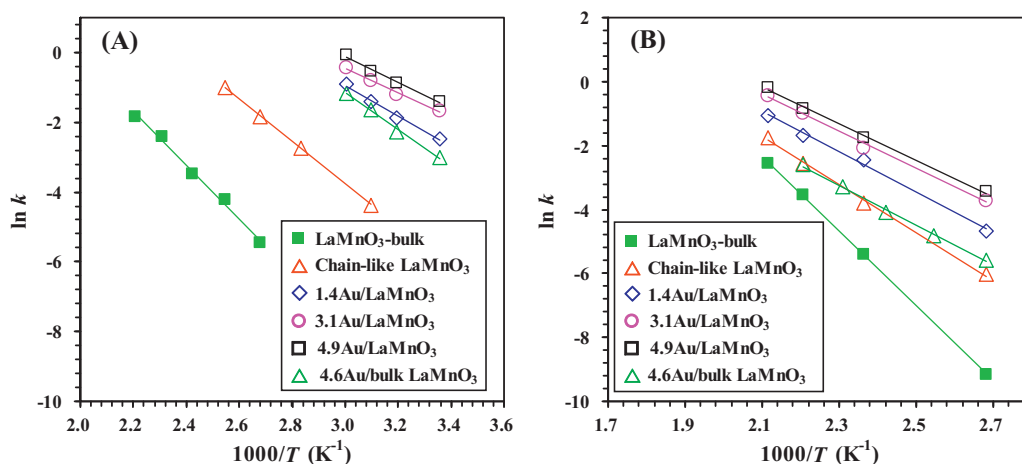
Fig. 8. The Arrhenius plots for the oxidation of (A) CO and (B) toluene over the $LaMnO_3$, xAu/$LaMnO_3$, and 4.6Au/bulk $LaMnO_3$ samples.

concentration [63]. Bondzie et al. found that the oxidation of CO over the Au/TiO_2 catalyst was first-order toward CO pressure and oxygen coverage [64]. Therefore, it is reasonable to suppose that the oxidation of CO and toluene in the presence of excess oxygen (CO/O_2 volume ratio = 1/20 and toluene/O_2 molar ratio = 1/400) would obey a first-order reaction mechanism with respect to CO or toluene concentration (c):

$$r = -kc = \left(-A \exp \left(-\frac{E_a}{RT} \right) \right) c$$

where r, k, A, and E_a are the reaction rate (mol/s), rate constant (s^{-1}), pre-exponential factor, and apparent activation energy (kJ/mol), respectively.

The Arrhenius plots for CO and toluene oxidation over the $LaMnO_3$ and xAu/$LaMnO_3$ samples are shown in Fig. 8, and their apparent activation energies are presented in Table 2. It can be observed that the E_a value for either CO oxidation or toluene combustion decreased in a sequence of $LaMnO_3$-bulk > chain-like $LaMnO_3$ > 4.6Au/bulk $LaMnO_3$ > 1.4Au/$LaMnO_3$ > 3.1Au/$LaMnO_3$ > 4.9Au/$LaMnO_3$, with the lower E_a values (29–37 and 47–52 kJ/mol, respectively) being achieved over the xAu/$LaMnO_3$ samples. Such a result suggests that CO and toluene oxidation might proceed more readily over the porous $LaMnO_3$ and Au-loaded porous $LaMnO_3$ samples. The striking difference in E_a can be likely related to the difference in the total number of active sites, which is directly related to the extent of exposed Au and $LaMnO_3$ surfaces and the presence of a strong Au–$LaMnO_3$ interaction.

Table S2 of the supplementary material summarizes the E_a values of various catalysts for CO and toluene oxidation reported in the literature. Obviously, the E_a values of the chain-like $LaMnO_3$ catalyst was much lower than those of the Al_2O_3-supported CuO or MnO_x [65] and $Ni_{0.5}Zn_{0.5}Fe_2O_4$ [66] catalysts for toluene combustion, similar to those of the 10–20 wt% $LaCoO_3$/$Ce_{1-x}Zr_xO_2$ (x = 0–0.2) [62] and 7 wt% Pt/16 wt% $Ce_{0.64}Zr_{0.15}Bi_{0.21}O_{1.895}$/γ-$Al_2O_3$ [67] catalysts for toluene combustion, and those of the $LaFeO_3$ [68] and $LaMnO_3$ [69] catalysts for CO oxidation, but higher than that of the α-Mn_2O_3 catalyst for CO oxidation [70]. The E_a values of the 3.1Au/$LaMnO_3$ catalyst was similar to those of the Au/TiO_2 [15], Au/Fe_2O_3 [71], and Au/Mn_2O_3 [70] catalysts, but lower than those of the Au/SiO_2 catalysts [72,73] for CO oxidation. Therefore, the results of kinetic investigations confirm that the chain-like $LaMnO_3$ and xAu/$LaMnO_3$ catalysts showed high catalytic performance for the oxidation of CO and toluene at low temperatures.

4. Conclusions

In summary, we have prepared the chain-like ordered macroporous $LaMnO_3$ and xAu/$LaMnO_3$ samples via the colloidal crystal-templating and gas bubble-assisted PVA-protected reduction methods, respectively. There were good correlations of O_{ads} concentration and low-temperature reducibility with catalytic activity of the samples for the oxidation of CO and toluene. Among the $LaMnO_3$ and xAu/$LaMnO_3$ samples, 4.9Au/$LaMnO_3$ performed the best, giving the $T_{50\%}$ and $T_{90\%}$ of 61 and 91 °C for CO oxidation, and of 201 and 226 °C for toluene combustion, respectively. The xAu/$LaMnO_3$ samples exhibited the apparent activation energies of 29–37 and 47–52 kJ/mol for the oxidation of CO and toluene, respectively. It is concluded that the high catalytic performance of 4.9Au/$LaMnO_3$ might be associated with its higher surface area and O_{ads} concentration and better low-temperature reducibility as well as the strong interaction between Au NPs and chain-like $LaMnO_3$ support.

Appendix A. Supplementary data

Supplementary data associated with this article can be found, in the online version, at http://dx.doi.org/10.1016/j.apcatb.2013.04.025.

References

[1] M.A. Peña, J.L.G. Fierro, Chemical Reviews 101 (2001) 1981–2018.
[2] A. Weidenkaff, Advanced Engineering Materials 6 (2004) 709–714.
[3] V. Blasin-Aubé, J. Belkouch, L. Monceaux, Applied Catalysis B 43 (2003) 175–186.

[4] B.P. Barbero, J.A. Gamboa, L.E. Cadus, Applied Catalysis B 65 (2006) 21–30.
[5] H. Taguchi, S. Yamasaki, A. Itadani, M. Yosinaga, K. Hirota, Catalysis Communications 9 (2008) 1913–1915.
[6] S.H. Liang, T.G. Xu, F. Teng, R.L. Zong, Y.F. Zhu, Applied Catalysis B 96 (2010) 267–275.
[7] F. Li, D.P. Josephson, A. Stein, Angewandte Chemie International Edition 50 (2011) 360–388.
[8] M. Sadakane, T. Horiuchi, N. Kato, C. Takahashi, W. Ueda, Chemistry of Materials 19 (2007) 5779–5785.
[9] H.W. Yan, C.F. Blanford, J.C. Lytle, C.B. Carter, W.H. Smyrl, A. Stein, Chemistry of Materials 13 (2001) 4314–4321.
[10] F. Li, Y.Q. Qian, A. Stein, Chemistry of Materials 22 (2010) 3226–3235.
[11] F. Li, Z.Y. Wang, A. Stein, Angewandte Chemie International Edition 46 (2007) 1885–1888.
[12] F. Li, S.A. Delo, A. Stein, Angewandte Chemie International Edition 46 (2007) 6666–6669.
[13] M. Haruta, T. Kobayashi, H. Sano, N. Yamada, Chemistry Letters 2 (1987) 405–408.
[14] B.K. Min, C.M. Friend, Chemical Reviews 107 (2007) 2709–2724.
[15] B.C. Liu, Y. Liu, C.Y. Li, W.T. Hu, P. Jing, Q. Wang, J. Zhang, Applied Catalysis B 127 (2012) 47–58.
[16] T.A. Ntho, J.A. Anderson, M.S. Scurrell, Journal of Catalysis 261 (2009) 94–100.
[17] G.J. Hutchings, M.S. Hall, A.F. Carley, P. Landon, B.E. Solsona, C.J. Kiely, A. Herzing, M. Makkee, J.A. Moulijn, A. Overweg, J.C. Fierro-Gonzalez, J. Guzman, B.C. Gates, Journal of Catalysis 242 (2006) 71–81.
[18] B.B. Chen, C. Shi, M. Crocker, Y. Wang, A.M. Zhu, Applied Catalysis B 132–133 (2013) 245–255.
[19] X. Zhang, H. Shi, B.Q. Xu, Angewandte Chemie International Edition 44 (2005) 7132–7135.
[20] L.C. Wang, Q. Liu, X.S. Huang, Y.M. Liu, Y. Cao, K.N. Fan, Applied Catalysis B 88 (2009) 204–212.
[21] S. Scirè, L.F. Liotta, Applied Catalysis B 125 (2012) 222–246.
[22] T. Barakat, J.C. Rooke, E. Genty, R. Cousin, S. Siffert, B.-L. Su, Energy and Environmental Science 6 (2013) 371–391.
[23] G.M. Veith, A.R. Lupini, S. Rashkeev, S.J. Pennycook, D.R. Mullins, V. Schwartz, C.A. Bridges, N.J. Dudney, Journal of Catalysis 262 (2009) 92–101.
[24] H.N. Li, L. Zhang, H.X. Dai, H. He, Inorganic Chemistry 48 (2009) 4421–4434.
[25] P. Ciambelli, S. Cimino, S.D. Rossi, M. Faticanti, L. Lisi, G. Minelli, I. Pettiti, P. Porta, G. Russo, M. Turco, Applied Catalysis B 24 (2000) 243–253.
[26] Y.F. Han, D. Kumar, C. Sivadinarayana, D.W. Goodman, Journal of Catalysis 224 (2004) 60–68.
[27] S. Ponce, M.A. Peña, J.L.G. Fierro, Applied Catalysis B 24 (2000) 193–205.
[28] A. Machocki, T. Ioannides, B. Stasinska, W. Gac, G. Avgouropoulos, D. Delimaris, W. Grzegorczyk, S. Pasieczna, Journal of Catalysis 227 (2004) 282–296.
[29] H. Taguchi, A. Sugita, M. Nagao, Journal of Solid State Chemistry 119 (1995) 164–168.
[30] Y.C. Wei, J. Liu, Z. Zhao, A.J. Duan, G.Y. Jiang, Journal of Catalysis 287 (2012) 13–29.
[31] Y.C. Wei, J. Liu, Z. Zhao, Y.S. Chen, C.M. Xu, A.J. Duan, G.Y. Jiang, H. He, Angewandte Chemie International Edition 50 (2011) 2326–2329.
[32] D.A. Bulushev, I. Yuranov, E.I. Suvorova, P.A. Buffat, L.K. Minsker, Journal of Catalysis 224 (2004) 8–17.
[33] J.C. Fierro-Gonzalez, B.C. Gates, Catalysis Today 122 (2007) 201–210.
[34] S.T. Daniells, A.R. Overweg, M. Makkee, J.A. Moulijn, Journal of Catalysis 230 (2005) 52–65.
[35] J.H. Chen, M.Q. Shen, X.Q. Wang, G.S. Qi, J. Wang, W. Li, Applied Catalysis B 134–135 (2013) 251–257.
[36] F. Teng, W. Han, S.H. Liang, B. Gaugeu, R.L. Zong, Y.F. Zhu, Journal of Catalysis 250 (2007) 1–11.
[37] R. Spinicci, M. Faticanti, P. Marini, S. De Rossi, P. Porta, Journal of Molecular Catalysis A 197 (2003) 147–155.
[38] H. Najjar, H. Batis, Applied Catalysis A 383 (2010) 192–201.
[39] K.D. Chen, S.B. Xie, A.T. Bell, E. Iglesia, Journal of Catalysis 198 (2001) 232–242.
[40] H.X. Dai, A.T. Bell, E. Iglesia, Journal of Catalysis 221 (2004) 491–499.
[41] S. Mukherjee, M.A. Vannice, Journal of Catalysis 243 (2006) 108–130.
[42] P.B. Weisz, C.D. Prater, Advances in Catalysis and Related Subjects 6 (1954) 143–196.
[43] J. Xu, L. Ouyang, W. Mao, X.J. Yang, X.C. Xu, J.J. Su, T.Z. Zhuang, H. Li, Y.F. Han, ACS Catalysis 2 (2012) 261–269.
[44] M.L. Jia, Menggentuya, Z. Bao, Y.N. Shen, Catalysis Letters 134 (2010) 87–92.
[45] M. Valden, X. Lai, D.W. Goodman, Science 281 (1998) 1647–1650.
[46] S.C. Kim, W.G. Shim, Applied Catalysis B 98 (2010) 180–185.
[47] N. Gunasekaran, S. Saddawi, J.J. Carberry, Journal of Catalysis 159 (1996) 107–111.
[48] F.N. Aguero, A. Scian, B.P. Barbero, L.E. Cadus, Catalysis Letters 128 (2008) 1–13.
[49] P. Papaefthimiou, T. Ioannides, X.E. Verykios, Catalysis Today 54 (1999) 81–92.
[50] S. Minico, S. Scire, C. Crisafulli, R. Maggiore, S. Galvagno, Applied Catalysis B 28 (2000) 245–251.
[51] M.A. Centeno, M. Paulis, M. Montes, J.A. Odriozola, Applied Catalysis A 234 (2002) 65–78.
[52] P. Mars, D.W. van Krevelen, Chemical Engineering Science (Supplement) 3 (1954) 41–59.
[53] K.A. Davis, D.W. Goodman, Journal of Physical Chemistry B 104 (2000) 8557–8562.
[54] G.C. Bond, D.T. Thompson, Catalysis Reviews: Science and Engineering 41 (1999) 319–388.
[55] S. Minico, S. Scire, C. Crisafulli, S. Galvagno, Applied Catalysis B 34 (2001) 277–285.
[56] C.-T. Wang, S.-H. Ro, Journal of Non-Crystalline Solids 352 (2006) 35–43.
[57] R.D. Waters, J.J. Weimer, J.E. Smith, Catalysis Letters 30 (1995) 181–188.
[58] M.P. Casaletto, A. Longo, A.M. Venezia, A. Martorana, A. Prestianni, Applied Catalysis A 302 (2006) 309–316.
[59] J. Guzman, B.C. Gates, Journal of the American Chemical Society 126 (2004) 2672–2673.
[60] Q. Ye, J.S. Zhao, F.F. Huo, D. Wang, S.Y. Cheng, T.F. Kang, H.X. Dai, Microporous and Mesoporous Materials 172 (2013) 20–29.
[61] C.T. Wong, A.Z. Abdullah, S. Bhatia, Journal of Hazardous Materials 157 (2008) 480–489.
[62] M. Alifanti, M. Florea, S. Somacescu, V.I. Pârvulescu, Applied Catalysis B 60 (2005) 33–39.
[63] A.P. Jia, G.S. Hu, L. Meng, Y.L. Xie, J.Q. Lu, M.F. Luo, Journal of Catalysis 289 (2012) 199–209.
[64] V.A. Bondzie, S.C. Parker, C.T. Campbell, Catalysis Letters 63 (1999) 143–151.
[65] S.M. Saqer, D.I. Kondarides, X.E. Verykios, Applied Catalysis B 103 (2011) 275–286.
[66] M. Florea, M. Alifanti, V.I. Pârvulescu, D. Mihaila-Tarabasanu, L. Diamandescu, M. Feder, C. Negrila, L. Frunza, Catalysis Today 141 (2009) 361–366.
[67] T. Masui, H. Imadzu, N. Matsuyama, N. Imanaka, Journal of Hazardous Materials 176 (2010) 1106–1109.
[68] P. Ciambelli, S. Cimino, S. De Rossi, L. Lisi, G. Minelli, P. Porta, G. Russo, Applied Catalysis B 29 (2001) 239–250.
[69] S. Cimino, S. Colonna, S. De Rossi, M. Faticanti, L. Lisi, I. Pettiti, P. Portaz, Journal of Catalysis 205 (2002) 309–317.
[70] L.C. Wang, X.S. Huang, Q. Liu, Y.M. Liu, Y. Cao, H.Y. He, K.N. Fan, J.H. Zhuang, Journal of Catalysis 259 (2008) 66–74.
[71] M.M. Schubert, S. Hackenberg, A.C. van Veen, M. Muhler, V. Plzak, R.J. Behm, Journal of Catalysis 197 (2001) 113–122.
[72] R.P. Doherty, J.-M. Krafft, C. Méthivier, S. Casale, H. Remita, C. Louis, C. Thomas, Journal of Catalysis 287 (2012) 102–113.
[73] J. Xu, T. White, P. Li, C.H. He, J.G. Yu, W.K. Yuan, Y.F. Han, Journal of the American Chemical Society 132 (2010) 10398–10406.